The fuzzy coat of pathological human Tau fibrils is a two-layered polyelectrolyte brush

Susanne Wegmann[a,b,1], Izhar D. Medalsy[a], Eckhard Mandelkow[c,d,e], and Daniel J. Müller[a,1]

[a]Department of Biosystems Science and Engineering, Eidgenössische Technische Hochschule Zürich, 4058 Basel, Switzerland; [b]Department of Neurology, Harvard Medical School and Alzheimer's Disease Research Laboratory, Massachusetts General Hospital, Charlestown, MA 02129; [c]German Center for Neurodegenerative Diseases, 53175 Bonn, Germany; [d]Center of Advanced European Studies and Research, 53175 Bonn, Germany; and [e]Max Planck Institute for Neurological Research Cologne, Hamburg Outstation, 22607 Hamburg, Germany

Edited by Ueli Aebi, University of Basel, Basel, Switzerland, and accepted by the Editorial Board November 21, 2012 (received for review July 18, 2012)

The structure and properties of amyloid-like Tau fibrils accumulating in neurodegenerative diseases have been debated for decades. Although the core of Tau fibrils assembles from short β-strands, the properties of the much longer unstructured Tau domains protruding from the fibril core remain largely obscure. Applying immunogold transmission EM, and force-volume atomic force microscopy (AFM), we imaged human Tau fibrils at high resolution and simultaneously mapped their mechanical and adhesive properties. Tau fibrils showed a ≈16-nm–thick fuzzy coat that resembles a two-layered polyelectrolyte brush, which is formed by the unstructured short C-terminal and long N-terminal Tau domains. The mechanical and adhesive properties of the fuzzy coat are modulated by electrolytes and pH, and thus by the cellular environment. These unique properties of the fuzzy coat help in understanding how Tau fibrils disturb cellular interactions and accumulate in neurofibrillary tangles.

protein aggregation | Alzheimer's disease | paired helical filaments

The pathological formation of fibrillar aggregates of human Tau proteins occurs in Alzheimer's disease, frontotemporal dementia, and other neurodegenerative diseases. In the human brain, six main isoforms of Tau are expressed, which bind and stabilize axonal microtubules (MTs) (1, 2). Binding of Tau to MTs is facilitated by four ≈31-aa long MT-binding pseudorepeats (R1 to R4) and their flanking regions. The ≈240-aa-long N-terminal domain (Fig. 1*A*) and the ≈70-aa-long C-terminal domain, which make up ≈70% of the longest human Tau protein, hTau40, remain unstructured (3) and project from the MT into the surrounding medium (4). Dissociation of Tau from MTs is induced by phosphorylation at multiple sites and by various kinases (5, reviewed in refs. 6, 7). Once dissociated from MTs, Tau can assemble into fibrillar aggregates, commonly referred to as paired helical filaments (PHFs) (8). Whereas β-stranded hexapeptide motifs facilitate the aggregation of Tau repeat domains (TauRDs) in the fibril core (9–12), the largely unstructured and flexible N- and C-terminal domains are thought to protrude from the fibril core (Fig. 1*A*). This model, in which the core of fibrillar Tau aggregates is surrounded by a "fuzzy coat," was inferred from early transmission EM (TEM) images of antibody-labeled Tau termini that partially projected from the fibril (13). However, to date, the structural heterogeneity of the Tau terminal domains has limited the characterization of the fuzzy coat by TEM and NMR (9, 14, 15), and various properties of the fuzzy coat are not quantified.

We previously used high-resolution atomic force microscopy (AFM) to observe the structural polymorphism of Tau fibrils in physiological solution (16). Fibrils of recombinant full-length hTau40 showed a thickness (i.e., height measured by AFM) of ≈18.5 nm, whereas the thickness of fibril cores assembled from recombinant TauRDs that lack most of the terminal Tau domains (Fig. 1*A*) was unexpectedly similar (≈15.9 nm). This suggests that the N- and C-terminal domains in hTau40 fibrils, which represent the majority of the Tau polypeptide, contribute only ≈2.6 nm to the fibril thickness. In contrast, if the unstructured terminal domains were to collapse onto the fibril core with dense packing of the polypeptide chains, they should occupy a volume that contributes at least ≈11 nm to the fibril thickness (17). Such packing of the terminal Tau domains would increase the overall Tau fibril thickness to ≈30 nm. This raises the question of which structural and physiochemical properties make the fuzzy coat largely "invisible" in AFM, TEM, and NMR. We tackled the challenge of visualizing the fuzzy coat of Tau fibrils by applying immunogold-TEM and high-resolution AFM in the force-volume mode (FV-AFM), which is particularly suited to imaging single biomolecules at much improved force sensitivity and to mapping their physicochemical properties at nanometer resolution (≈1–2 nm) simultaneously (18, 19). With immunogold-TEM and high-resolution FV-AFM, we could directly image and map the properties of the fuzzy coat of single Tau fibrils. Our results reveal that the fuzzy coat of hTau40 fibrils resembles a ≈16-nm–thick, negatively charged, two-layered polyelectrolyte brush, which changes mechanical and adhesive properties with pH and electrolytes. Depending on the physiological conditions, the fuzzy coat gradually changes properties, ranging from mechanically stiff and repulsive to mechanically flexible and adhesive. This responsiveness of the fuzzy coat suggests that changes in the brain physiology, such as those occurring with age and in neurodegenerative diseases, modulate the mechanical stability of Tau fibrils, alter the interactions between Tau fibrils and proteins, and influence the aggregation propensity of Tau fibrils in vitro and in vivo.

Results and Discussion

Human Full-Length Tau Fibrils Carry a Mechanically Soft, Weakly Adhesive Fuzzy Coat. The structural properties of the flexible terminal Tau domains from amyloid-like Tau fibrils are largely unknown (13, 20). Immunogold-TEM images of full-length Tau fibrils, in which the N- and C-terminal Tau domains were labeled with gold-conjugated antibodies (21), suggested that the terminal Tau ends protrude from the fibrils and form a fuzzy coat around the rigid fibril core that consists of stacked TauRDs (Fig. 1*A*). Limited trypsin digestion of human full-length hTau40 fibrils removes the fuzzy coat and leaves behind the fibril core (Fig. 1 *B* and *C*). Immunogold-TEM of human Tau fibrils (Fig. 1 *D*–*F*) confirmed that trypsin digestion removed the labeling of the N-terminal Tau domains by gold-conjugated antibodies. To characterize the fuzzy coat directly, we deposited fibrils assembled from recombinant TauRDs (Fig. 2 *A* and *B*) and then from full-length Tau (Fig. 2 *A*

Author contributions: S.W. and D.J.M. designed research; S.W. and I.D.M. performed research; E.M. contributed new reagents/analytic tools; S.W., I.D.M., E.M., and D.J.M. analyzed data; and S.W., I.D.M., E.M., and D.J.M. wrote the paper.

The authors declare no conflict of interest.

This article is a PNAS Direct Submission. U.A. is a guest editor invited by the Editorial Board.

Freely available online through the PNAS open access option.

[1]To whom correspondence may be addressed. E-mail: daniel.mueller@bsse.ethz.ch or susanne.wegmann@partners.org.

See Author Summary on page 1156 (volume 110, number 4).

This article contains supporting information online at www.pnas.org/lookup/suppl/doi:10.1073/pnas.1212100110/-/DCSupplemental.

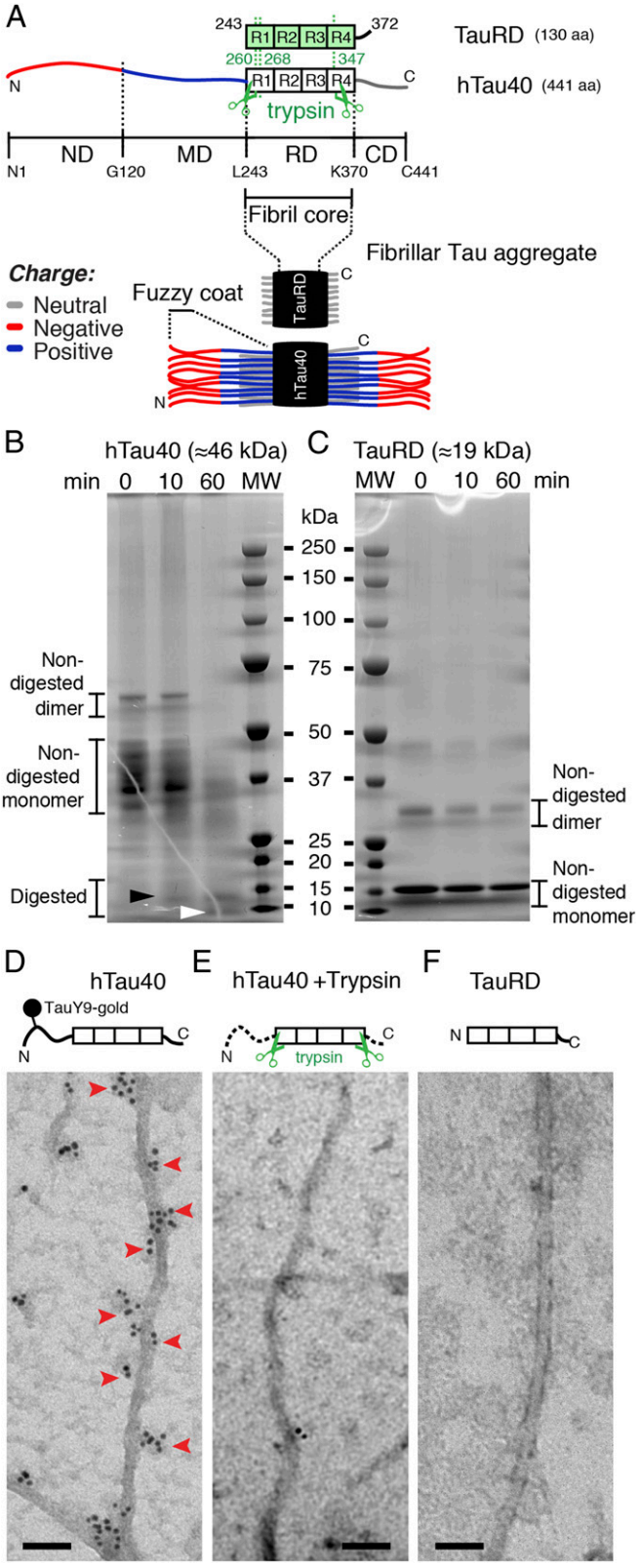

Fig. 1. Trypsin digestion suggests a fuzzy coat of Tau fibrils. (*A*) Longest hTau40 isoform (441 aa) consists of an RD (amino acids 244–370) with four pseudorepeats (R1 to R4) that is flanked by flexible ND (amino acids 1–120), MD (amino acids 121–243), and CD (amino acids 371–441). The RD construct (TauRD, 130 aa) of hTau40 mostly consists of the four pseudorepeats. Limited trypsin digestion of hTau40 fibrils removes the ND (260/268 aa) and CD (93 aa) (3). In fibrillar Tau aggregates, the fibril core consists of a stack of TauRDs, whereas the N and C termini are thought to protrude brush-like to form the "fuzzy coat." SDS/PAGE of hTau40 (*B*, ≈46 kDa) and TauRD (*C*, ≈19 kDa) fibrils after limited digestion with trypsin (molar ratio Tau/trypsin = 600:1) for 0 (not digested), 10, and 60 min. Limited trypsin digestion reduces the apparent molecular mass of hTau40 from ≈46 kDa to ≈9–12 kDa (3). Nondigested hTau40 fibrils (0 min) contained full-length Tau with different migrating properties. After 10 min of incubation with trypsin, truncated species occur (black arrowhead). Efficient removal of the termini from hTau40 fibrils was achieved after 60 min of incubation (white arrowhead). Nondigested TauRD fibrils (0 min) showed the same molecular mass (≈19 kDa) as TauRD fibrils after short (10 min) and long (60 min) trypsin digestion. MW, molecular weight marker. TEM of hTau40 fibrils (*D*) and TauRD fibrils (*F*) that were immunogold-labeled using a primary antibody (TauY9, epitope aa 12–27) against the ND of hTau40 and a gold-labeled secondary antibody (*Materials and Methods*). (*D*) Immunolabeling of the ND (red arrowheads) occurred on alternating sides of hTau40 fibrils and apparently followed the fibril twist. Immunolabeling did not occur in TauRD fibrils (*F*) and trypsin-digested hTau40 fibrils (*E*), which both lack the N-terminal end of hTau40. (Scale bars: *D*–*F*, 50 nm.)

and *C*) on the same mica support and imaged the fibrils in buffer solution by FV-AFM. For every pixel of the AFM topography, FV-AFM approaches the AFM stylus to the sample and records a force-distance curve (Fig. S1) from which the mechanical deformation (Fig. 2*D*) and adhesion (Fig. 2*E*) of the sample are extracted. FV-AFM topographs (Fig. 2*C*) recorded at imaging forces of 300 pN at pH 7.4 in presence of 50 mM KCl showed the typical appearance of TauRD fibrils and hTau40 fibrils (16). Cross-sections taken perpendicular to the fibril center (Fig. 2*I*) revealed a height of 7.2 ± 3.2 nm [mean ± SD (n = 49)] for TauRD fibrils and of 13.6 ± 3.3 nm (n = 87) for hTau40 fibrils (Table 1). The height difference between TauRD and hTau40 fibrils suggested that the terminal domains of hTau40 contributed 6.4 nm to the fibril thickness. However, the height and width of hTau40 fibrils depended on the imaging force at which the AFM stylus was pushed onto the sample (Fig. S2). When decreasing the imaging force to 50 pN, the hTau40 fibrils increased in height to 16.2 ± 7.8 nm (n = 24), but when the imaging force was increased to 400 pN, the fibrils decreased in height to 10.5 ± 3.0 nm (n = 22). This force-induced deformation of hTau40 fibrils was fully reversible. In contrast, the height of fibrils assembled from the TauRD fibrils only depended much less on imaging forces and ranged from 9.4 ± 3.9 nm (n = 24) at 50 pN to 7.2 ± 1.2 nm (n = 20) at 400 pN.

Deformation maps showed that at an imaging force of 300 pN, the AFM stylus compressed TauRD fibrils by 0.7 ± 0.4 nm (n = 35) and hTau40 fibrils by 2.9 ± 1.5 nm (n = 53) (Fig. 2*D* and Table 1). The maximum deformation of TauRD fibrils occurred at a distance of 7.2 ± 1.2 nm (n = 29) from the fibril center (Fig. 2*J*), and that of hTau40 fibrils occurred at a distance of 11.8 ± 2.8 nm (n = 32) from the fibril center. In contrast to TauRD fibrils, the deformation of hTau40 fibrils sensitively depended on the imaging forces (Fig. S2). At imaging forces of 100 pN, lanes of maximum deformation run at a distance of ≈19.2 nm parallel to the fibril center (Figs. S2*C* and S3). Because both hTau40 and TauRD fibrils are assumed to have a similar core of stacked repeat domains (RDs) (22, 23) (Fig. 1*A*), we conclude that the deformation lanes running parallel to the hTau40 fibril cores resulted from the fuzzy coat. The fuzzy coat is extended at low imaging forces and becomes successively compressed when increasing the imaging forces of the AFM stylus. From the deformation, we can approximate the spring constants of hTau40 (k = 0.10 N/m) and TauRD (k = 0.43 N/m) fibrils (Table 1). These spring constants suggest that the fuzzy coat is mechanically up to four times softer than the fibril core and forms a soft cushion around hTau40 fibrils.

Adhesion maps revealed a smaller adhesion of the AFM stylus to hTau40 fibrils [19.6 ± 6.1 pN (n = 50)] compared with TauRD fibrils [38.7 ± 14.7 pN (n = 40)] (Fig. 2 *E* and *K* and Table 1). Because the AFM stylus is hydrophilic, is negatively charged,

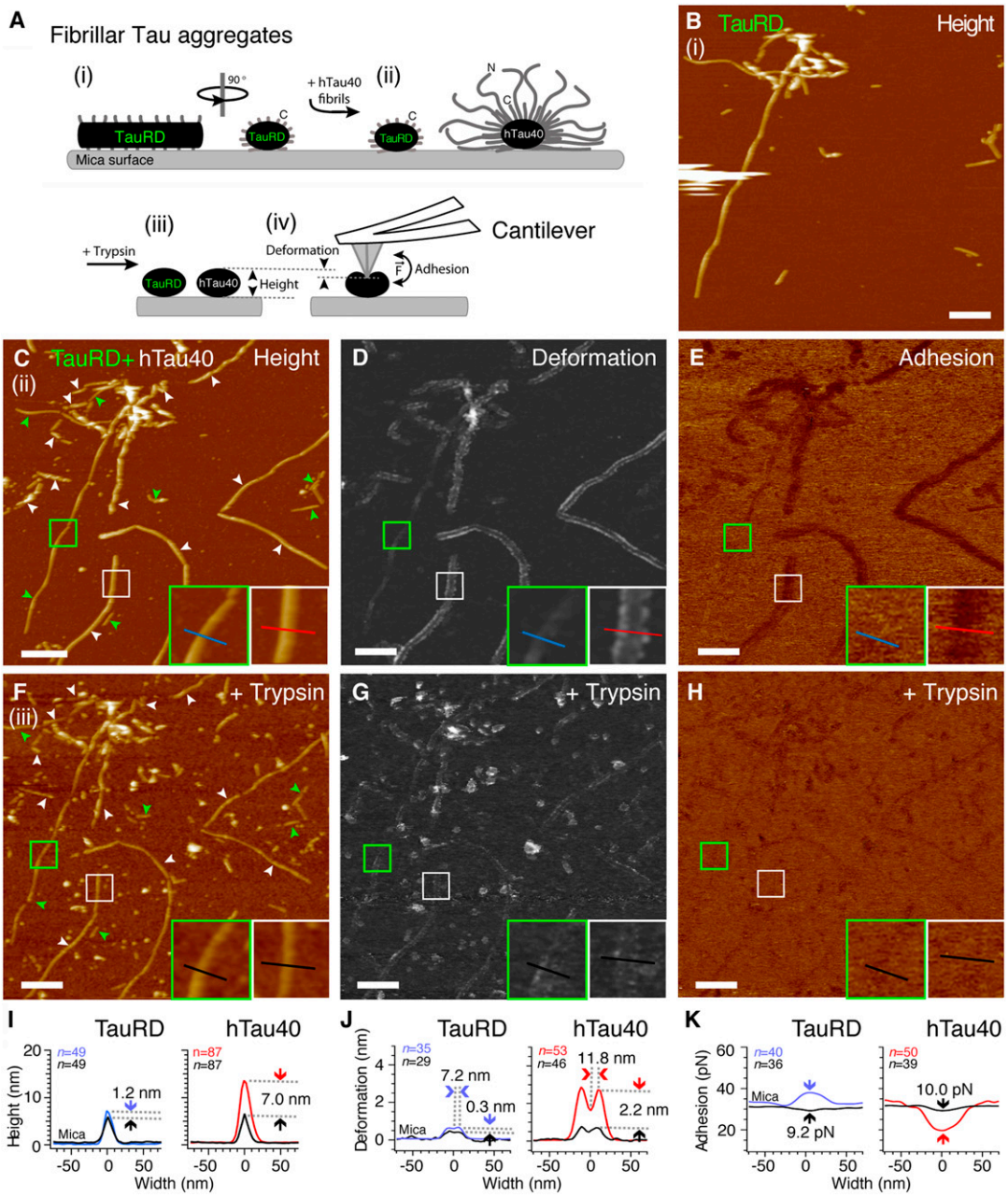

Fig. 2. Detecting the fuzzy coat of hTau40 fibrils by FV-AFM imaging. (*A*) TauRD fibrils (*i*) and hTau40 fibrils (*ii*) were coadsorbed onto mica and imaged by FV-AFM. (*iii*) After trypsin digestion of the fuzzy coat, the same TauRD and hTau40 fibrils were measured again (*iv*) and the fibril height, deformation, and adhesion were compared with previous nondigested conditions. (*B*) AFM topography of TauRD fibrils adsorbed onto mica. (*C*) AFM topography of hTau40 fibrils (white arrowheads) and TauRD fibrils (green arrowheads) coadsorbed onto mica. (*Insets*) Close-ups of TauRD (green frame) and hTau40 (white frame) fibrils and lines indicate cross-section profiles measured perpendicular to the fibril core. (*D*) Deformation map of Tau fibrils indented by the AFM stylus. (*Insets*) Same regions as in *C*. (*E*) Adhesion force map recorded between the AFM stylus and the Tau fibrils. Topography (*F*), deformation (*G*), and adhesion (*H*) maps of Tau fibrils imaged in *C*–*E* but recorded after incubation in 1 mg/mL trypsin solution are shown. (*Insets*) Close-ups of the same TauRD fibrils (green frame) and hTau40 fibrils (white frame) as imaged in *C*–*E*. Average height (*I*), deformation (*J*), and adhesion (*K*) cross-sections of TauRD and hTau40 fibrils recorded before (colored lines) and after (black lines) trypsin digestion are shown. Trypsin digestion changes fibril height (*I*), deformation (*J*), and adhesion (*K*). Maximum deformation of undigested fibrils occurred parallel to the fibril center at a distance of 11.8 nm in hTau40 fibrils and at a distance of 7.2 nm in TauRD fibrils (arrows). Full-range color scales correspond to a height of 40 nm (*B*, *C*, and *F*), deformation of 15 nm (*D* and *G*), and adhesion force of 150 pN (*E* and *H*). (Scale bars: *B*–*H*, 200 nm.)

and has a diameter (≈2–5 nm) similar to many cytoplasmic proteins, one can assume that the AFM stylus mimics unspecific electrostatic interactions of proteins with Tau fibrils (24). Compared with "naked" TauRD fibrils devoid of the fuzzy coat, the AFM stylus shows lower adhesion to hTau40 fibrils surrounded by a fuzzy coat. This reduced adhesion indicates that the fuzzy coat reduces the adhesion of negative-charged proteins to hTau40 fibrils.

Fuzzy Coat Modulates Mechanical and Adhesive Properties of Tau Fibrils. To verify that the high deformation and low adhesion of hTau40 fibrils compared with TauRD fibrils originated from the

Table 1. Mean height, deformation, and adhesion of TauRD and hTau40 fibrils in different conditions

	pH	KCl	Height, nm (mean ± SD)	*n*	*P* value		Deformation, nm (mean ± SD)	*n*	*P* value		Fuzzy coat spring constant, N/m	Adhesion, pN (mean ± SD)	*n*	*P* value	
TauRD	7.4	50 mM	7.2 ± 3.2	49	←		0.7 ± 0.4	35	←		0.43	38.7 ± 14.7	40	←	
TauRD + trypsin	7.4	50 mM	6.0 ± 2.6	49	0.04	←	0.4 ± 0.5	29	0.01	←	0.75	29.5 ± 4.5	36	0.00	←
hTau40	7.4	50 mM	13.6 ± 3.3	87	←		2.9 ± 1.5	53	←		0.1	19.6 ± 6.1	50	←	
hTau40 + trypsin	7.4	50 mM	6.6 ± 2.6	87	0.00	0.20	0.7 ± 0.9	46	0.00	0.07	0.43	29.5 ± 3.0	39	0.00	1.00
hTau40	7.4	200 mM	12.9 ± 3.8	36	←	←	5.5 ± 2.7	36	←	←	0.05	21.5 ± 3.9	37	←	←
hTau40	7.4	10 mM	12.9 ± 3.5	41	1.00	1.00	1.4 ± 0.7	44	0.00	0.00	0.21	19.4 ± 5.4	54	0.03	0.03
hTau40	9.5	200 mM	13.1 ± 4.3	34	0.84	←	3.4 ± 1.7	40	0.00	←	0.09	20.0 ± 4.0	42	0.10	←
hTau40	9.5	10 mM	14.2 ± 4.5	43	0.17	0.29	2.3 ± 1.3	42	0.00	0.00	0.13	19.7 ± 5.6	45	0.09	0.77
hTau40	4.5	200 mM	13.6 ± 4.5	39	0.47	←	3.1 ± 1.4	31	0.00	←	0.1	32.8 ± 6.0	28	0.00	←
hTau40	4.5	10 mM	14.0 ± 4.6	41	0.25	0.70	1.4 ± 0.5	34	0.00	0.00	0.21	74.9 ± 28.9	45	0.00	0.00
hTau40	7.4	Intracell*	12.8 ± 2.0	30	0.89		2.6 ± 0.9	22	0.00		0.12	21.4 ± 5.6	29	0.94	

Mean values (±SD) of the maximum height, deformation, and adhesion force determined from cross-sections (Figs. S4 and S5) of TauRD and hTau40 fibrils before and after digestion with trypsin. hTau40 fibrils were also characterized at pH 4.5, pH 7.4, and pH 9.5, each in 10 mM and 200 mM KCl. Statistical significance (*P* values) of the difference between mean values was determined applying two-tailed Student *t* tests. Arrows indicate the reference value for each *P* value given below the arrow. Statistical significance was assumed for $P < 0.05$. The number of cross-sections analyzed is given by *n*. Spring constants of the fuzzy coat were determined by dividing the FV-AFM imaging force through the deformation. All data were recorded using FV-AFM at an imaging force of 300 pN. *Intracellular buffer: 150 mM KCl, 12 mM NaCl, and 0.8 mM $CaCl_2$ (pH 7.4).

fuzzy coat, we enzymatically removed the terminal Tau domains (Fig. 1 *B* and *C*). Limited trypsin digestion of Tau fibrils removes most of the N- and C-terminal domains, leaving behind the RDs forming the fibril core (3). After limited proteolysis, the same fibrils were imaged using identical AFM parameters as before proteolysis (Fig. 2 *F*–*H*). The height of TauRD fibrils decreased by 1.2 nm, whereas the height of hTau40 fibrils decreased by 7.0 nm (Fig. 2*I*). The pronounced deformation lanes running parallel to the hTau40 fibril core disappeared after trypsin digestion (Fig. 2*J*). Furthermore, trypsin digestion increased the adhesion of the AFM stylus to hTau40 fibrils to that of digested TauRD fibrils (Fig. 2 *H* and *K* and Table 1). In summary, the differences in height, deformation, and adhesion between TauRD and hTau40 fibrils were removed by limited trypsin digestion (Table 1 and Fig. S4) and hTau40 and TauRD fibrils showed equal structural, mechanical, and adhesive properties. These experimental results confirmed the existence and highlighted the unique structural properties of a relatively thick fuzzy coat surrounding hTau40 fibrils. Subtracting the radius (half-height after trypsin digestion) of the hTau40 fibril core ≈3.0–3.3 nm (Table 1) from the maximal distance of the deformation lanes ≈19 nm running parallel to the fibril hTau40 core (Figs. S2*C* and S3), we estimate the maximal thickness of the fuzzy coat to be ≈16 nm.

Stiffness of the Fuzzy Coat Depends on Electrolyte Concentration. The net charge of the terminal hTau40 domains forming the fuzzy coat varies with the pH of the buffer solution (Fig. 3*A* and Table S1). From pH 4–10, the acidic N-terminal tail domain (ND; residues 1–120) is negatively charged; the basic middle domain (MD) and the RD are positively charged; and the C-terminal tail domain (CD; residues ≈370–441) is neutral at pH 7.4, positive at pH 4.5, and negative at pH 9.5 (25). At pH 7.4, the N terminus of hTau40 possesses an excess of negative charges (−8), whereas the CD contains no net charge. To test whether this unequal charge distribution of the Tau termini changes the structural properties of the fuzzy coat, we reimaged the same hTau40 fibrils (Fig. 3*B*) at different pH values and electrolyte concentrations. Imaging forces of 300 pN were applied to ensure sufficient interaction of the AFM stylus with the fuzzy coat. At pH 7.4 and 10 mM KCl (Fig. 3*C*), hTau40 fibrils had a height of 12.9 ± 3.5 nm ($n = 41$) and the fuzzy coat deformed 1.4 ± 0.7 nm ($n = 44$) (Table 1 and Fig. S5). When increasing the ion concentration to 200 mM KCl (Fig. 3 *D* and *E*), the fibril height remained unchanged [12.9 ± 3.8 nm ($n = 36$)] but the deformation of the fuzzy coat increased [5.5 ± 2.7 nm ($n = 36$)]. Thus, when increasing the electrolyte concentration, the fuzzy coat of hTau40 fibrils became ≈fourfold mechanically softer ($k = 0.21$ N/m in 10 mM KCl, $k = 0.05$ N/m in 200 mM KCl; Table 1). This electrolyte-dependent mechanical softening of the fuzzy coat could be observed for all pH values tested (Fig. 3 *C*–*K* and Table 1). Changing the pH to 4.5 (Fig. 3 *F*–*H*) or to 9.5 (Fig. 3 *I*–*K*) induced only minor changes in hTau40 fibril height compared with pH 7.4 (Table 1). Interestingly, in intracellular buffer (pH 7.4, 150 mM KCl, 12 mM NaCl, 0.8 mM $CaCl_2$), the deformation of hTau40 fibrils decreased and the fuzzy coat stiffened compared with hTau40 fibrils characterized at pH 7.4 in 200 mM KCl ($k =$ 0.12 N/m) (Table 1 and Fig. S5). This stiffening of the fuzzy coat is attributed to the interplay of monovalent and divalent ions (26). In summary, we could show that the mechanical properties of the fuzzy coat that surrounds hTau40 fibrils sensitively depend on the electrolyte concentration of the buffer solution. In general, the fuzzy coat mechanically stiffens when reducing the electrolytes.

Adhesion of the Fuzzy Coat Depends on pH. The adhesion of the negatively charged, hydrophilic AFM stylus to the fuzzy coat can mimic interactions between Tau fibrils and negatively charged hydrophilic biomolecules (24), such as tubulin (≈4–5 nm in diameter), the main interaction partner of Tau (27, 28). At pH 7.4, the AFM stylus adhered at ≈20 pN to hTau40 fibrils independent of the ion concentration (Fig. 3 *C*–*E* and Table 1). High-resolution FV-AFM images (Fig. 4) show that the lowest adhesion is established in lanes parallel to the hTau40 fibril core. Superimposing the deformation and the adhesion maps shows that both correlate structurally with each other (Fig. 4*D*). Because the fuzzy coat mainly contributes to the characteristic deformation lines of hTau40 fibrils, these results indicate that at physiological pH 7.4, negatively charged molecules are weakly attracted by the fuzzy coat.

At pH 9.5, only two cysteines of the fibril core (C291 and C322; $pK_a = 8.1$) deprotonate, and the net charge of the terminal hTau40 domains remains similar to that at pH 7.4 (Fig. 3*A*). Accordingly, at pH 9.5, the adhesion remained the same as observed for pH 7.4 (≈20 pN) and was independent of the ion concentration (Fig. 3 *I* and *J* and Table 1). However, at pH 4.5, the terminal hTau40 domains contain many more positive than negative charges, such that the net charge of the fuzzy coat becomes positive (Fig. 3*A*). Apart from the numerous lysines ($pK_a = 10.7$) and arginines ($pK_a =$ 12.1), the major contribution to the positive charges originates from protonated histidines ($pK_a = 6.0$) in the ND (H14, H32, and H94) and the CD (H384, H397, and H416). Accordingly, at pH 4.5 (10 mM KCl), the adhesion between the fuzzy coat and AFM stylus increased ≈fourfold from 19.4 ± 5.4 pN (pH 7.4,

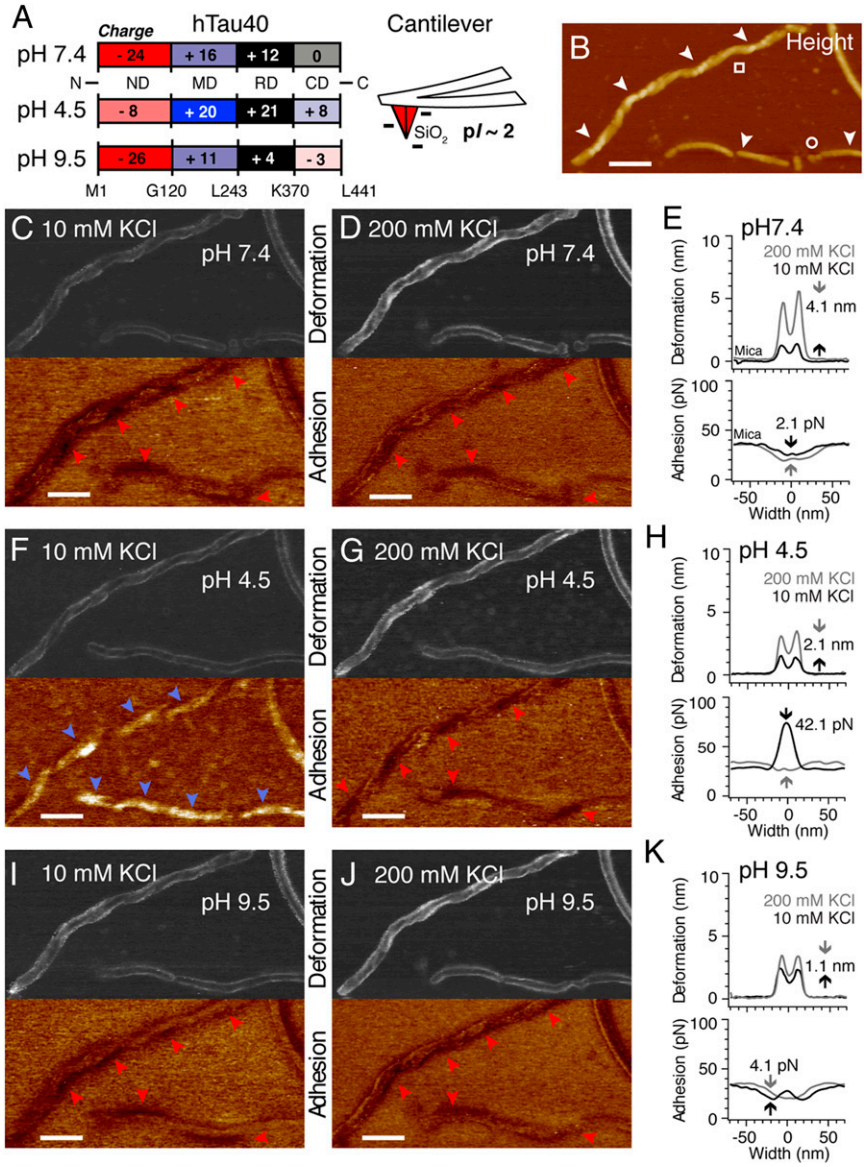

Fig. 3. Electrolyte- and pH-dependent properties of the fuzzy coat. (*A*) pH-dependent net charge of RD, MD, ND, and CD in monomeric hTau40. The SiO_2 AFM stylus has an isoelectric point (p*I*) of about 2 and is negatively charged at pH >2. (*B*) AFM topography recorded at pH 7.4 in 10 mM KCl shows twisted (□) and smooth (○) hTau40 fibrils. Deformation and adhesion maps recorded at pH 7.5 in 10 mM KCl (*C*) and 200 mM KCl (*D*) are shown. Adhesion minima (red arrowheads) occur at the periphery of hTau40 fibrils and match the fibril twisting. (*E*) Averaged deformation (*Upper*) and adhesion (*Lower*) cross-section profiles of hTau40 fibrils at pH 7.4 in 10 mM KCl (black line) and 200 mM KCl (gray line). Increasing the salt concentration from 10 to 200 mM KCl increases deformation by 4.1 nm and decreases adhesion by 2.1 pN. (*F*) Deformation and adhesion maps recorded at pH 4.5 in 10 mM KCl. Adhesion maxima (blue arrowheads) occur along the fibril backbone. (*G*) Deformation and adhesion maps recorded at pH 4.5 in 200 mM KCl. Adhesion minima (red arrowheads) occur along the fibrillar core. (*H*) Average deformation and adhesion cross-section profiles of hTau40 fibrils at pH 4.5 in 10 mM KCl (black line) and 200 mM KCl (gray line). Increasing the salt concentration from 10 to 200 mM KCl increases the deformation by 2.1 nm and decreases the adhesion by 42.1 pN. Deformation and adhesion maps were recorded at pH 9.5 in 10 mM KCl (*I*) and 200 mM KCl (*J*). Adhesion minima (red arrowheads) occur at the same positions as recorded at pH 7.4 in *C* and *D*. (*K*) Average deformation and adhesion cross-section profiles at pH 9.5 in 10 mM KCl (black line) and 200 mM KCl (gray line). Increasing the ion concentration from 10 to 200 mM KCl increases deformation by 1.1 nm and adhesion by 4.1 pN. (Scale bars: 100 nm.)

10 mM KCl) to 74.9 ± 28.9 pN (n = 45) (Fig. 3 *F* and *H*). This pH-dependent increase in adhesion disappeared when increasing the ion concentration to 200 mM KCl (Fig. 3 *G* and *H* and Table 1). Thus, it may be concluded that the increased adhesion at pH 4.5 originates from electrostatic attractions between the negatively charged AFM stylus and the positively charged MDs and CDs (Fig. 3*A*). In summary, these experiments suggest that at low pH, the fuzzy coat increases the adhesion of Tau fibrils to negatively charged biomolecules and could function as an electrostatic trap.

Terminal Tau Domains Forming the Fuzzy Coat Change Arrangement with Fibril Morphology. The adhesive map of twisted hTau40 fibrils recorded at pH 4.5 revealed adhesion maxima in 10 mM KCl (Fig. 3*F*) and local adhesion minima in 200 mM KCl (Fig. 3*G*) that alternated along the fibril. At pH 7.4, regions of low adhesion were independent of the ion concentration and ran parallel to the fibril core (Fig. 3 *C* and *D*). However, at pH 4.5, pH 7.4, and pH 9.5, as well as in conditions mimicking intracellular pH and ion composition, the fuzzy coat showed heterogeneous adhesive distributions along twisted fibrils. In straight hTau40 fibrils (Fig. 4*A*), regions of

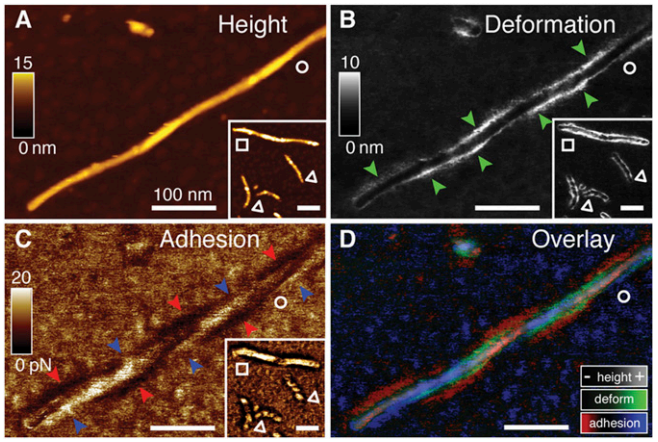

Fig. 4. Properties of the fuzzy coat depend on the twist of the Tau fibril. (*A*) AFM topographs recorded at very low imaging forces (≈35 pN) in PBS, pH 7.4, show the polymorphic twist and morphology (*Inset*) of hTau40 fibrils: thick twisted (□), thin twisted (△), and thin straight (○) fibrils. (*B*) Enhanced deformation is detected on both sides of thick twisted (□) and thin twisted (△) fibrils. In thin straight fibrils (○), enhanced deformation (green arrowheads) alternates along the sides of the fibril. (*C*) Regions of minimum (blue arrowheads) and maximum (red arrowheads) adhesion alternate along the twisted hTau40 fibril. (*D*) Overlay of topography, deformation, and adhesion maps. Enhanced deformation (green) and low adhesion (red) alternate along the twisted hTau40 fibril. Enhanced adhesion (blue) is detected opposite to low adhesion and enhanced deformation. (Scale bars: 100 nm.)

low and high adhesion (Fig. 4*C*) localized to opposite sides of the fibril and their distribution depended on the fibril twist. High deformation (Fig. 4*B*) occurred at sites of low adhesion (Fig. 4*D*). Because the ND of hTau40 is negatively charged at pH 7.4 (Fig. 3*A*), it should expose the lowest adhesion to the negatively charged AFM stylus. The asymmetrical distribution of adhesion minima along twisted and straight hTau40 fibrils suggests that the NDs protrude sideways from hTau40 fibrils (i.e., parallel to the mica support), where they expose high structural flexibility. Such an arrangement of NDs in the fuzzy coat would be consistent with a parallel β-strand stacking of Tau molecules in the fibril backbone (12, 23). In this case, all N-terminal ends protrude to the same side in straight fibrils and form a twist-dependent brush surrounding twisted fibrils. However, the assembly of Tau molecules may vary among Tau fibrils, thereby inducing a high degree of structural polymorphism (16).

Fuzzy Coat of Tau Fibrils: Two-Layered Polyelectrolyte Brush. Our experiments revealed that full-length hTau40 fibrils are surrounded by a fuzzy coat that is ≈16 nm thick. The fuzzy coat is established by terminal Tau domains (ND, MD, and CD) that structurally extend from the core of the Tau fibril. Based on these insights, we suggest a polymer brush model of the fuzzy coat surrounding hTau40 fibrils (Fig. 5). The packing of four Tau molecules per nanometer of fibril core (3) suggests a dense grafting of the unstructured Tau terminal domains protruding from the fibril core. In the absence of terminal domains, the core of Tau fibrils has a diameter (height) of ≈6.0–6.6 nm (Table 1). To account for the curvature of the grafting surface formed by the fuzzy coat of Tau fibrils, a spherical polymer brush model is applied (29), in which the radial decrease in polymer density reduces the brush thickness. Our FV-AFM measurements quantified the force-dependent deformation and high mechanical flexibility of the fuzzy coat. Similarly, NMR of full-length Tau fibrils revealed that the structural flexibility of the Tau N termini increases with distance to the fibril core (15). From these results, and because the ND and CD have quite different lengths (Fig. 1*A*), one may consider the fuzzy coat of hTau40 fibrils to be a two-layered cylindrical polyelectrolyte brush that consists of charged polypeptide chains and surrounds the Tau fibril core (Fig. 5*A* and Fig. S6). In this model, the dense inner and mechanically more rigid polymer brush layer is formed by the CD and parts of the MDs (≈amino acids 173–243) that protrude ≈70 aa (≈8 nm) from the fibril core (Fig. 5*B*). Beyond this distance (>70 aa), a second less dense and mechanically more flexible polymer brush layer is formed by the remaining ≈170 aa of the longer NDs. From spherical or cylindrical polymer brush models (29), one can expect that a two-layered polyelectrolyte brush formed by the Tau termini has a thickness of ≈13 to ≈16 nm (Fig. 5*B* and Fig. S6). This model of a two-layered polyelectrolyte brush describes the up to ≈16-nm–thick fuzzy coat observed for hTau40 fibrils; however, it does not consider the complex charge distribution along the termini.

Properties and Biological Consequences of the Fuzzy Coat Model. At physiological conditions (pH 7.4, 10–200 mM monovalent ions) the ND of Tau carries net negative charges (Fig. 3*A*) and forms a ≈16-nm–thick, brush-like polypeptide coat that determines mechanical and adhesive properties of the hTau40 fibril (Fig. 5 *A* and *B*). These properties, which are determined by the fuzzy coat of the hTau40 fibril, depend on ion concentration, ion composition, and pH (Fig. 5*C*). Increasing the ion concentration screens repulsive electrostatic forces between the Tau termini and decreases the fuzzy coat stiffness by ≈50% (Fig. 3 *C–E* and Table 1). Because the overall charge of the fuzzy coat is negative, its adhesion to negatively charged particles and molecules is rather weak. Lowering the pH charges the fuzzy coat positive and increases the adhesion to negatively charged particles (Fig. 3 *C* and *F* and Table 1). Therefore, one may speculate that Tau fibrils significantly change their adhesive properties when exposed to low pH during lysosomal degradation (30). An analogous change in adhesion may explain the interactions between full-length Tau and lipid membranes of different surface charges (31). At low pH, a large part of the increased adhesion can be screened, increasing the ion concentration of the buffer solution. The fuzzy coat of Tau fibrils thus shows characteristics of a grafted, anionic polyelectrolyte brush (26). A similar electrolyte-sensitive brush of polypeptide chains is suggested to transmit interactions between neurofilaments (32, 33). In the case of neurofilaments, phosphorylation of the polypeptide chains increases the number of negative charges in the polypeptide brush. The additional charges lead to an electrostatic repulsion between polypeptide chains forming the brush, and thus to a volume increase of neurofilament brushes. This volume exclusion regulates neurofilament spacing. Similarly, the pH- and electrolyte-induced tuning of the mechanical and adhesive properties of the fuzzy coat of Tau fibrils may play a role in vivo in determining the rigidity, stability, and bundling of fibrillar Tau aggregates. The posttranslational modifications of Tau, such as pathological hyperphosphorylation (7, 34), glycosylation (35), and nitration (36), introduce negative charges at numerous sites of the Tau termini. Furthermore, truncation of the C terminus by Caspase-3 (37) and of the N terminus by calpain (38, 39) removes parts of the fuzzy coat. Such recharging and cleavage of the Tau termini alters the polyelectrolyte brush-like properties of the fuzzy coat. Consequently, Tau fibrils would alter their mechanical and adhesive properties and determine their role in neurodegenerative diseases.

At intracellular buffer conditions (Table 1 and Fig. S5), the fuzzy coat was stiffer than at comparable pH (7.4) and monovalent ion concentration (≈200 mM). It is likely that the fuzzy coat contributes to the pronounced stability of pathological intracellular Tau fibrils, which can accumulate in neurofibrillar tangles over years. Remarkably, at low ion concentrations (≤50 mM KCl) that soften the fuzzy coat, Tau fibrils on hydrophobic surfaces become unstable and spontaneously disassemble into smaller subunits (16). In vivo, the softening of the fuzzy coat could trigger fibril fragmentation and formation of the soluble Tau oligomers that are widely discussed as toxic (40, 41) and transmissive (42, 43) species in tauopathies.

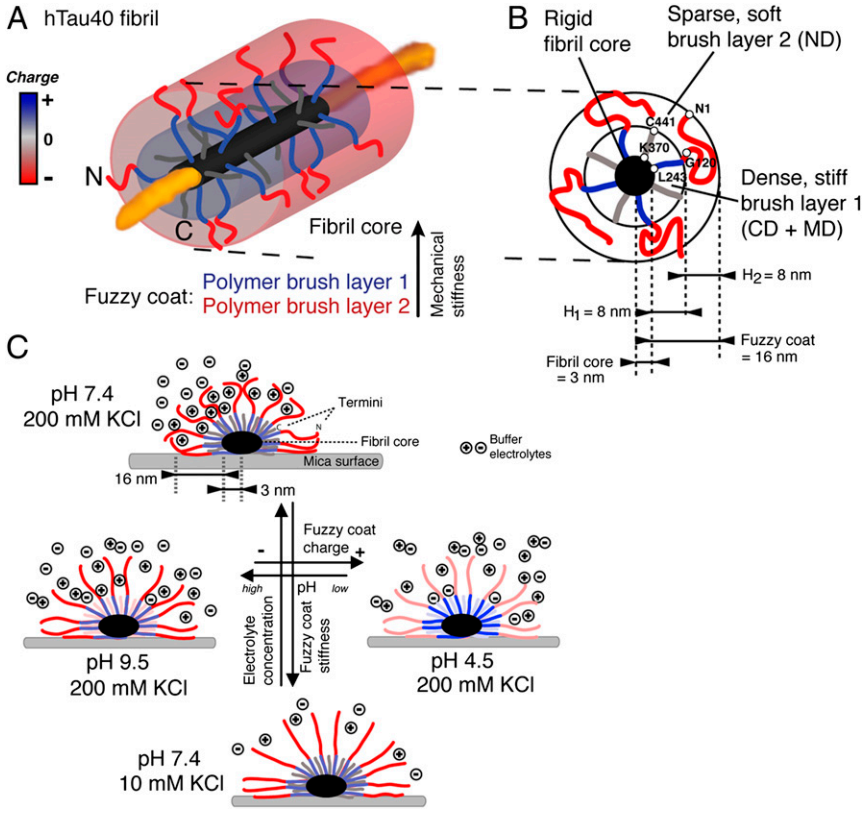

Fig. 5. Two-layered polyelectrolyte brush model of the fuzzy coat surrounding Tau fibrils. (*A*) Model of a Tau fibril being covered by a two-layered polyelectrolyte brush. (*B*) Section through hTau40 fibril with four Tau molecules (eight terminal domains) per nanometer of fibril length. The fuzzy coat of hTau40 fibrils forms a ≈16-nm–thick two-layered polyelectrolyte brush that protrudes from the ≈6-nm–thick fibril core into the surrounding medium. Double approximate 70 aa of the CD (amino acids 370–440) and the MD (amino acids 120–243) cover the fibril core and form an ≈8-nm–thick dense layer. A second outer sparse layer, formed by the further extension of ≈170 residues of the ND (amino acids 1–120) and part of the MD shows a thickness of ≈8 nm. (*C*) At pH 7.4, 200 mM KCl (*Upper*) partly shields the negative charges, and thus the electrostatic repulsion between the termini. This shielding enhances the structural flexibility of the termini and reduces the mechanical rigidity of the fuzzy coat. Decreasing the ionic concentration to 10 mM KCl (*Lower*) increases the electrostatic repulsion between the charged Tau termini. This leads to a decrease in mechanical flexibility and stiffens the fuzzy coat. Simultaneously, the adhesion of the fuzzy coat to negatively charged molecules decreases. Changing the pH to 9.5 (*Left*) or to 4.5 (*Right*) charges the fuzzy coat negative or positive, respectively. Accordingly, the fuzzy coat changes mechanical properties and electrostatic adhesion with the environment. A detailed calculation of parameters characterizing the two-layered polyelectrolyte brush model is given in Fig. S6.

When bound to MTs, the terminal domains of Tau project from the MT surface (4) in a highly flexible manner (15, 44), and may thus also expose polyelectrolyte brush-like behavior. In this case, it is debated whether the projecting Tau termini act as spacers (45) or linkers (46) between MTs. The grafting density of Tau polypeptides protruding from the MT surface is considerably lower compared with that observed for Tau fibrils. Thus, the polyelectrolyte brush of Tau on MTs may show quite different properties, especially if further modified by the flexible acidic C-terminal tubulin tails that also protrude from the MT surface (47) and can be regarded as a disordered polymer brush. Nevertheless, a pH and ion concentration-dependent softening of Tau termini brushes on MTs could have a considerable impact on MT stability, stiffness, interactions, and MT bundling (48–50).

Materials and Methods

Tau Protein Expression. Full-length hTau40 (2N4R, 441 residues, molecular mass ≈45.9 kDa) and TauRD construct (construct K18, 130 residues, molecular mass ≈18.8 kDa) (Fig. 1*A*) were expressed in *Escherichia coli*. Purification was achieved by heat treatment and FPLC Mono S chromatography (Amersham Biosciences) as described (51). The purity of the proteins was analyzed by SDS/PAGE. Protein concentrations were determined by absorbance at 214 nm. The pH-dependent charges of the acidic (amino acids M1–L243) parts of the N-terminal end and the C-terminal end (amino acids K369–L441) (25) were calculated using PROTEIN CALCULATOR v3.3 (The Scripps Research Institute) (Table S1).

Tau Fibril Preparation. Aggregation of Tau into fibrils was induced by incubating 50 μM soluble hTau40 or TauRD in volumes of 20 μL at 37 °C in 20 mM N,N-Bis-(2-hydroxyethyl)-2-amino-ethansulfonic acid (BES), pH 7.4, plus 25 mM NaCl buffer containing the anionic cofactor heparin 6,000 (average molecular mass ≈6,000 Da; Sigma; molar ratio of Tau to heparin ≈4:1) for incubation times of ≈3 d for TauRD or ≈6–7 d for hTau40. Formation of aggregates was ascertained by Thioflavine S fluorescence and EM (52).

Immunogold-TEM. For immunogold labeling of NDs, 5 μL of the Tau fibril preparation specified was diluted in PBS (final Tau concentration ≈2.7 μM) and adsorbed on carbon-coated EM grids (Electron Microscopy Science) for 20 min. Excess protein was removed by placing EM grids three times on drops of fresh PBS. After blocking in 1% (wt/vol) BSA in PBS for 60 min, grids were incubated with primary anti-Tau antibody (rabbit TauY9, epitope amino acids 12–27 of the ND; Enzo Life Science) diluted 1:200 in 1% BSA for 1 h. After being washed five times in PBS, grids were incubated in gold-labeled secondary antibody (donkey anti-rabbit 6-nm gold; Aurion) diluted 1:20 in 1% BSA for 60 min, followed by five washes in PBS. Postfixation was done in fresh 1% (wt/vol) glutaraldehyde in PBS for 3 min and by subsequent excessive washing in water. The sample was negatively stained by incubation in 2% (wt/vol) uranyl-acetate in water two times for 8 min each time, followed by brief washing in water and 10 min of drying at 23 °C. Tau fibrils were imaged by TEM (JEM-1011; JEOL).

Sample Preparation for AFM. Thirty microliters of a Tau fibril preparation diluted in PBS (final Tau concentration ≈5 μM) was placed on freshly cleaved mica and incubated for 20–25 min at 23 °C. Excess protein was removed by ex-

changing the sample solution against fresh imaging buffer for a total of eight times. AFM imaging buffers were prepared using ultrapure water and adjusted to pH 4.5 (10 mM NaAcetate; Sigma), pH 7.4 (10 mM Tris; Sigma), and pH 9.5 (10 mM Tris) using HCl. Ion concentrations added were 10 mM, 50 mM, or 200 mM KCl (Fluka). Intracellular buffer contained 150 mM KCl, 12 mM NaCl, and 0.8 mM $CaCl_2$ at pH 7.4. After exchanging the buffer, the sample was equilibrated for 20 min at 23 °C. To image TauRD and hTau40 fibrils deposited on the same surface, we first deposited, imaged, and identified TauRD fibrils. Afterward, we deposited a similar amount of hTau40 fibrils on top of the TauRD fibrils and reimaged the same surface area (Fig. 2 *B* and *C*). All experiments were repeated at least three times. To exclude imaging artifacts when comparing TauRD fibrils with hTau40 fibrils and hTau40 fibrils in different pH and electrolyte conditions, we used the same AFM stylus.

Limited Trypsin Digestion of Tau Fibrils. For limited trypsin digestion of TauRD and hTau40 fibrils, Tau fibrils (≈15 mg) in PBS were incubated with trypsin (molar ratio of Tau/trypsin ≈600:1) at 37 °C for 10 min and 60 min (3). Proteolysis was stopped by addition of SDS/PAGE sample buffer, followed by boiling (95 °C for 5 min). Tau protein masses were analyzed by SDS/PAGE in 4–12% Tris·glycine gels (Invitrogen) using Mops-SDS running buffer followed by Coomassie staining (Fig. 1 *B* and *C*). Tau fibrils (≈10 mg) adsorbed to mica were digested by incubation in 1 mg/mL trypsin (Sigma) for 15 min at 23 °C (molar ratio of Tau/trypsin ≈1:1). Compared with trypsin digestion in solution, a 600-fold higher trypsin concentration was used to digest Tau fibrils adsorbed onto mica to account for the nonspecific immobilization of trypsin on mica. To stop proteolysis, the trypsin buffer was replaced 10 times by 50 mL of AFM imaging buffer. The appearance and nanomechanical properties of Tau fibrils did not change during subsequent AFM imaging for >1 h, indicating that remaining trypsin activity could be neglected. For EM, Tau fibrils were digested before adsorption to EM grids with 0.1 mg/mL trypsin in PBS for 3 min at 37 °C and digestion was stopped by addition of protease inhibitor mixture (Complete; Roche) and immediate adsorption to EM grids.

FV-AFM. FV-AFM images were recorded with a Nanoscope Multimode 8 (Bruker) equipped with a 120-μm piezoelectric scanner. AFM cantilevers (Scanasyst-Fluid+; Bruker) had nominal spring constants of ≈0.7 N/m, had resonance frequencies of ≈35 kHz in buffer, and carried a SiO_2 stylus with a nominal apex radius of ≈2 nm. High-resolution images with enhanced force sensitivity (Fig. 4 and Fig. S3) were recorded using cantilevers with nominal spring constants of ≈0.03 N/m and resonance frequencies of ≈30 kHz in buffer. Images were taken at scan rates of 0.2–0.8 Hz and a sampling rate of 2 kHz. For each pixel of the AFM topography (512 × 512 pixels), an approach and retraction force-distance curve (Fig. S1) was recorded. The AFM stylus was vertically oscillated at amplitudes of ≈20 nm. At the lowest point of the downward movement (approach), the stylus touched the sample surface with a preset maximum contact force, called imaging force. The force-feedback loop regulates the stylus sample distance to maintain the imaging force, and the height of the sample was recorded to reconstruct the height of each pixel in the AFM topography. When reaching the imaging force, the stylus movement was reversed to generate the retract force-distance curve (Fig. S1 *A* and *C*). Force-distance curves were low-pass-filtered (10 kHz) to remove thermal noise. Stylus sample deformation was calculated from approach force-distance curves. The sample deformation is defined as the stylus sample separation (nanometers) during which the AFM stylus is in contact with the sample while approaching. Compression/deformation of the stiff stylus (≈150 GPa) can be neglected when interacting with soft biological samples (≈20 MPa). For each approach force-distance curve, the deformation is calculated as the distance (nanometers) between the start and the end of the repulsive (positive) force regime (Fig. S1*B*). The adhesion force is the minimum force of the retraction force-distance curve (Fig. S1*C*). Topography, deformation, and adhesion images were processed using built-in processing tools. Cross-section profiles were measured using ImageJ v1.43 (National Institutes of Health) and analyzed and plotted using Igor Pro v6.22A (Wavemetrics). Spring constants of fuzzy coat and fibril core were calculated k = imaging force/deformation.

Statistical Analysis. The significance ($P < 0.05$) of changes in height, deformation, and adhesion of the fuzzy coat in different buffer conditions (Table 1) was tested by a two-tailed Student's t test assuming a normal distribution of the data.

ACKNOWLEDGMENTS. We thank J. Helenius, E. M. Mandelkow, B. T. Hyman, and T. Spires-Jones for critical discussions, and S. Chinnathambi and P. Bosshart for experimental assistance. We also thank M. DiFiglia and the Philly Dake EM center at the Massassachusetts General Hospital for support. This work was supported by the European Molecular Biology Organization, Eidgenössiche Technische Hochschule, Deutsche Forschungsgemeinschaft, Max-Planck-Gesellschaft, Deutsches Zentrum für Neurodegenerative Erkrankungen, and Swiss National Science Foundation.

1. Cleveland DW, Hwo SY, Kirschner MW (1977) Physical and chemical properties of purified tau factor and the role of tau in microtubule assembly. *J Mol Biol* 116(2): 227–247.
2. Goedert M, Wischik CM, Crowther RA, Walker JE, Klug A (1988) Cloning and sequencing of the cDNA encoding a core protein of the paired helical filament of Alzheimer disease: Identification as the microtubule-associated protein tau. *Proc Natl Acad Sci USA* 85(11):4051–4055.
3. von Bergen M, et al. (2006) The core of tau-paired helical filaments studied by scanning transmission electron microscopy and limited proteolysis. *Biochemistry* 45 (20):6446–6457.
4. Steiner B, et al. (1990) Phosphorylation of microtubule-associated protein tau: Identification of the site for Ca2(+)-calmodulin dependent kinase and relationship with tau phosphorylation in Alzheimer tangles. *EMBO J* 9(11):3539–3544.
5. Drewes G, Ebneth A, Preuss U, Mandelkow EM, Mandelkow E (1997) MARK, a novel family of protein kinases that phosphorylate microtubule-associated proteins and trigger microtubule disruption. *Cell* 89(2):297–308.
6. Dolan PJ, Johnson GV (2010) The role of tau kinases in Alzheimer's disease. *Curr Opin Drug Discov Devel* 13(5):595–603.
7. Hanger DP, Anderton BH, Noble W (2009) Tau phosphorylation: The therapeutic challenge for neurodegenerative disease. *Trends Mol Med* 15(3):112–119.
8. Kidd M (1963) Paired helical filaments in electron microscopy of Alzheimer's disease. *Nature* 197:192–193.
9. Barghorn S, Davies P, Mandelkow E (2004) Tau paired helical filaments from Alzheimer's disease brain and assembled in vitro are based on beta-structure in the core domain. *Biochemistry* 43(6):1694–1703.
10. Berriman J, et al. (2003) Tau filaments from human brain and from in vitro assembly of recombinant protein show cross-beta structure. *Proc Natl Acad Sci USA* 100(15): 9034–9038.
11. Inouye H, Sharma D, Goux WJ, Kirschner DA (2006) Structure of core domain of fibril-forming PHF/Tau fragments. *Biophys J* 90(5):1774–1789.
12. Margittai M, Langen R (2004) Template-assisted filament growth by parallel stacking of tau. *Proc Natl Acad Sci USA* 101(28):10278–10283.
13. Wischik CM, et al. (1988) Structural characterization of the core of the paired helical filament of Alzheimer disease. *Proc Natl Acad Sci USA* 85(13):4884–4888.
14. Mukrasch MD, et al. (2009) Structural polymorphism of 441-residue tau at single residue resolution. *PLoS Biol* 7(2):e34.
15. Sillen A, et al. (2005) Regions of tau implicated in the paired helical fragment core as defined by NMR. *Chembiochem* 6(10):1849–1856.
16. Wegmann S, et al. (2010) Human Tau isoforms assemble into ribbon-like fibrils that display polymorphic structure and stability. *J Biol Chem* 285(35):27302–27313.
17. deGennes P-G (1980) Conformations of polymers attached to an interface. *Macromolecules* 13(5):1069–1075.
18. Medalsy I, Hensen U, Muller DJ (2011) Imaging and quantifying chemical and physical properties of native proteins at molecular resolution by force-volume AFM. *Angew Chem Int Ed Engl* 50(50):12103–12108.
19. Adamcik J, Berquand A, Mezzenga R (2011) Single-step direct measurement of amyloid fibrils stiffness by peak force quantitative nanomechanical atomic force microscopy. *Appl Phys Lett* 98(19):193701–193703.
20. Bibow S, et al. (2011) The dynamic structure of filamentous tau. *Angew Chem Int Ed Engl* 50(48):11520–11524.
21. Ksiezak-Reding H, Yen SH (1991) Structural stability of paired helical filaments requires microtubule-binding domains of tau: A model for self-association. *Neuron* 6 (5):717–728.
22. von Bergen M, Barghorn S, Biernat J, Mandelkow EM, Mandelkow E (2005) Tau aggregation is driven by a transition from random coil to beta sheet structure. *Biochim Biophys Acta* 1739(2-3):158–166.
23. Daebel V, et al. (2012) β-Sheet core of tau paired helical filaments revealed by solid-state NMR. *J Am Chem Soc* 134(34):13982–13989.
24. Bright JN, Woolf TB, Hoh JH (2001) Predicting properties of intrinsically unstructured proteins. *Prog Biophys Mol Biol* 76(3):131–173.
25. Gustke N, Trinczek B, Biernat J, Mandelkow EM, Mandelkow E (1994) Domains of tau protein and interactions with microtubules. *Biochemistry* 33(32):9511–9522.
26. Ballauff M (2007) Spherical polyelectrolyte brushes. *Prog Polym Sci* 32(10):1135–1151.
27. Cleveland DW, Hwo SY, Kirschner MW (1977) Purification of tau, a microtubule-associated protein that induces assembly of microtubules from purified tubulin. *J Mol Biol* 116(2):207–225.
28. Drubin DG, Kirschner MW (1986) Tau protein function in living cells. *J Cell Biol* 103(6 Pt 2):2739–2746.
29. Dukes D, et al. (2010) Conformational transitions of spherical polymer brushes: Synthesis, characterization, and theory. *Macromolecules* 43(3):1564–1570.
30. Wang Y, et al. (2009) Tau fragmentation, aggregation and clearance: The dual role of lysosomal processing. *Hum Mol Genet* 18(21):4153–4170.

31. Jones EM, et al. (2012) Interaction of tau protein with model lipid membranes induces tau structural compaction and membrane disruption. *Biochemistry* 51(12):2539–2550.
32. Brown HG, Hoh JH (1997) Entropic exclusion by neurofilament sidearms: A mechanism for maintaining interfilament spacing. *Biochemistry* 36(49):15035–15040.
33. Kumar S, Hoh JH (2004) Modulation of repulsive forces between neurofilaments by sidearm phosphorylation. *Biochem Biophys Res Commun* 324(2):489–496.
34. Illenberger S, et al. (1998) The endogenous and cell cycle-dependent phosphorylation of tau protein in living cells: Implications for Alzheimer's disease. *Mol Biol Cell* 9(6): 1495–1512.
35. Yuzwa SA, et al. (2008) A potent mechanism-inspired O-GlcNAcase inhibitor that blocks phosphorylation of tau in vivo. *Nat Chem Biol* 4(8):483–490.
36. Reynolds MR, Berry RW, Binder LI (2005) Site-specific nitration and oxidative dityrosine bridging of the tau protein by peroxynitrite: implications for Alzheimer's disease. *Biochemistry* 44(5):1690–1700.
37. Cotman CW, Poon WW, Rissman RA, Blurton-Jones M (2005) The role of caspase cleavage of tau in Alzheimer disease neuropathology. *J Neuropathol Exp Neurol* 64 (2):104–112.
38. Garg S, Timm T, Mandelkow EM, Mandelkow E, Wang Y (2011) Cleavage of Tau by calpain in Alzheimer's disease: The quest for the toxic 17 kD fragment. *Neurobiol Aging* 32(1):1–14.
39. Park SY, Ferreira A (2005) The generation of a 17 kDa neurotoxic fragment: An alternative mechanism by which tau mediates beta-amyloid-induced neurodegeneration. *J Neurosci* 25(22):5365–5375.
40. Fox LM, et al. (2011) Soluble tau species, not neurofibrillary aggregates, disrupt neural system integration in a tau transgenic model. *J Neuropathol Exp Neurol* 70(7): 588–595.
41. Ward SM, Himmelstein DS, Lancia JK, Binder LI (2012) Tau oligomers and tau toxicity in neurodegenerative disease. *Biochem Soc Trans* 40(4):667–671.
42. de Calignon A, et al. (2012) Propagation of tau pathology in a model of early Alzheimer's disease. *Neuron* 73(4):685–697.
43. Liu L, et al. (2012) Trans-synaptic spread of tau pathology in vivo. *PLoS ONE* 7(2): e31302.
44. Woody RW, Clark DC, Roberts GC, Martin SR, Bayley PM (1983) Molecular flexibility in microtubule proteins: proton nuclear magnetic resonance characterization. *Biochemistry* 22(9):2186–2192.
45. Marx A, Pless J, Mandelkow EM, Mandelkow E (2000) On the rigidity of the cytoskeleton: Are MAPs crosslinkers or spacers of microtubules? *Cell Mol Biol (Noisy-le-grand)* 46(5):949–965.
46. Chen J, Kanai Y, Cowan NJ, Hirokawa N (1992) Projection domains of MAP2 and tau determine spacings between microtubules in dendrites and axons. *Nature* 360(6405): 674–677.
47. Nogales E, Wolf SG, Downing KH (1998) Structure of the alpha beta tubulin dimer by electron crystallography. *Nature* 391(6663):199–203.
48. Felgner H, et al. (1997) Domains of neuronal microtubule-associated proteins and flexural rigidity of microtubules. *J Cell Biol* 138(5):1067–1075.
49. Kanai Y, Chen JG, Hirokawa N (1992) Microtubule bundling by tau proteins in vivo: Analysis of functional domains. *EMBO J* 11(11):3953–3961.
50. Rosenberg KJ, Ross JL, Feinstein HE, Feinstein SC, Israelachvili J (2008) Complementary dimerization of microtubule-associated tau protein: Implications for microtubule bundling and tau-mediated pathogenesis. *Proc Natl Acad Sci USA* 105(21):7445–7450.
51. Barghorn S, Biernat J, Mandelkow E (2005) Purification of recombinant tau protein and preparation of Alzheimer-paired helical filaments in vitro. *Methods Mol Biol* 299: 35–51.
52. Friedhoff P, Schneider A, Mandelkow EM, Mandelkow E (1998) Rapid assembly of Alzheimer-like paired helical filaments from microtubule-associated protein tau monitored by fluorescence in solution. *Biochemistry* 37(28):10223–10230.